

# Microfabricated bolometer based on a vertically aligned carbon nanotube absorber

Anna Vaskuri<sup>a</sup>, Michelle S. Stephens<sup>a</sup>, Nathan A. Tomlin<sup>a</sup>, Christopher S. Yung<sup>a</sup>, Andrew J. Walowitz<sup>a</sup>, Cameron Straatsma<sup>b</sup>, David Harber<sup>b</sup>, and John H. Lehman<sup>a</sup>

<sup>a</sup>Applied Physics Division, National Institute of Standards and Technology, Broadway 325, Boulder, CO 80305, USA

<sup>b</sup>Laboratory for Atmospheric and Space Physics, University of Colorado, 1234 Innovation Dr., Boulder, CO 80303, USA

## ABSTRACT

We have designed a microfabricated planar absolute radiometer based on a vertically aligned carbon nanotube (VACNT) absorber and an electrical power substitution method. The radiometer is designed to operate at room temperature and to be capable of measuring laser powers up to 300 mW from 300 nm to 2300 nm with an expected expanded uncertainty of 0.06% ( $k = 2$ ). The electrical power substitution capability makes the radiometer absolute and traceable to the international system (SI) of units. The new bolometer is currently under construction and will replace NIST's 50 year old detector standard for free-space CW laser power measurements. We also study the possibility of reducing background temperature sensitivity by optimizing the spectral selectivity of the VACNT forest with a photonic crystal structure.

**Keywords:** Radiometer, bolometer, laser power, primary standard, background compensation, carbon nanotubes, photonic structure, spectral selectivity

## 1. INTRODUCTION

Development of extremely black vertically aligned carbon nanotube (VACNT) forests<sup>1</sup> has enabled replacing traditional cavity structures<sup>2,3</sup> used in bolometers with VACNT planar absorbers.<sup>4,5</sup> This enables microfabrication, and thus reduced mass, which provides faster response time. Bolometers can be operated at room temperature or at cryogenic temperatures. Cooling a bolometric detector to cryogenic temperatures has traditionally been preferred for high precision measurements as radiative losses become negligible, heat capacity of materials decreases, and certain materials become electrical superconductors at cryogenic temperatures.<sup>4-6</sup> Conversely, room temperature operation would allow for increased ease of operation. However, the radiative conductance is proportional to the third power of the absolute temperature ( $G_{\text{rad}} \propto T^3$ ), which at room temperature leads to an increased coupling between an absorber and its surrounding environment. This means that in addition to the laser beam power, the bolometer measures temperature variations of the room, which deteriorates the signal to noise ratio of a bolometer reading. Thus, differential methods have been developed where a similar detector chip is used for compensating temperature fluctuations of the environment, that is, common modes seen by both detectors.<sup>7,8</sup> With a spectrally selective absorber the radiometer would be much less sensitive to temperature fluctuations, removing the need of an additional background compensation detector chip.

At NIST, the existing 50 year old room temperature detector standard for free-space CW laser power measurements, commonly known as the C-series calorimeter,<sup>2,3</sup> can perform calibrations with an expanded uncertainty of 0.86% having a coverage factor  $k = 2$  which corresponds to the confidence level of approximately 95%. One measurement cycle of the C-series calorimeter takes approximately 15 minutes. Although the C-series calorimeter has served excellently, with modern absorber materials, electronics, and optimization tools, it is possible to build a replacement thermal detector with a faster response and an order of magnitude lower uncertainty. In this work, we have designed a new bolometer called the planar absolute radiometer for room temperature (PARRoT)

---

Further author information: Send correspondence to Anna Vaskuri  
E-mail: anna.vaskuri@nist.gov

to replace the old C-series calorimeter. The operating principle of a bolometer differs from that of a calorimeter; a bolometer measures laser power ( $W$ ) directly, whereas a calorimeter measures laser energy ( $J = W \cdot s$ ) from which the laser power can be determined from a known measurement time. PARRoT must meet the following performance criteria: linear closed-loop laser power detection from a few  $\mu W$  to 300 mW at laser wavelengths from 300 nm to 2300 nm with a closed-loop settling time less than 60 s. In addition, the absorber diameter has to be at least 20 mm for measuring beam diameters as large as 11 mm ( $1/e^2$ ). PARRoT has to be insensitive to the polarization of the laser beam to be measured, its spatial uniformity must be  $<0.02\%$  near the center of the absorber so that small misalignment from the center spot would not matter, and the measurement uncertainty has to be  $<0.1\%$  ( $k = 2$ ) at room temperature operation. The design of PARRoT is introduced in Section 2 and its estimated uncertainty budget in laser power measurements in Section 3. An inspiration to PARRoT's design came from the compact total irradiance monitor (CTIM) detector<sup>8</sup> which is a CubeSat instrument that has been developed in the joint project by LASP and NIST. Section 4 describes our efforts to develop a spectrally selective absorber. Conclusions are discussed in Section 5.

## 2. BOLOMETER DESIGN

A modeled assembly of the PARRoT radiometer is presented in Fig. 1. PARRoT has two identical detector chips: one for measuring the laser power and another for common mode suppression arising from room temperature fluctuations. In practice, the background measuring detector will be heated to 303 K by constant electrical power and the measuring detector will be feedback controlled with DC current by matching the temperatures of the two detector chips. Since the measuring detector chip is forced to follow the temperature of the background measuring detector chip, the laser power is measured as the difference in the electrical powers measured at two time intervals when the laser beam is on and when it is off. The base plate made of copper where both detector chips are connected via weak thermal links will be temperature-stabilized to 293 K with Peltier cooling. The PID parameters for closed loop controlling of the base plate temperature and the measuring detector chip temperature are optimized using Ziegler–Nichols tuning<sup>9</sup> from open-loop step response measurements. The closed loops will be controlled and the bolometer measurements acquired by a LabVIEW\* FPGA (field-programmable gate array) board. The radiometer is placed inside a vacuum chamber to avoid cooling of the absorber by convection. Optical access is provided by an uncoated fused silica window with a wedge angle of  $0.5^\circ$  and diameter of 76.2 mm. Both detector chips see the same window to ensure that the background compensation works properly. The laser power measured with the PARRoT radiometer is traceable to electrical power and the international system (SI) of units via the calibrated resistance of a standard resistor.

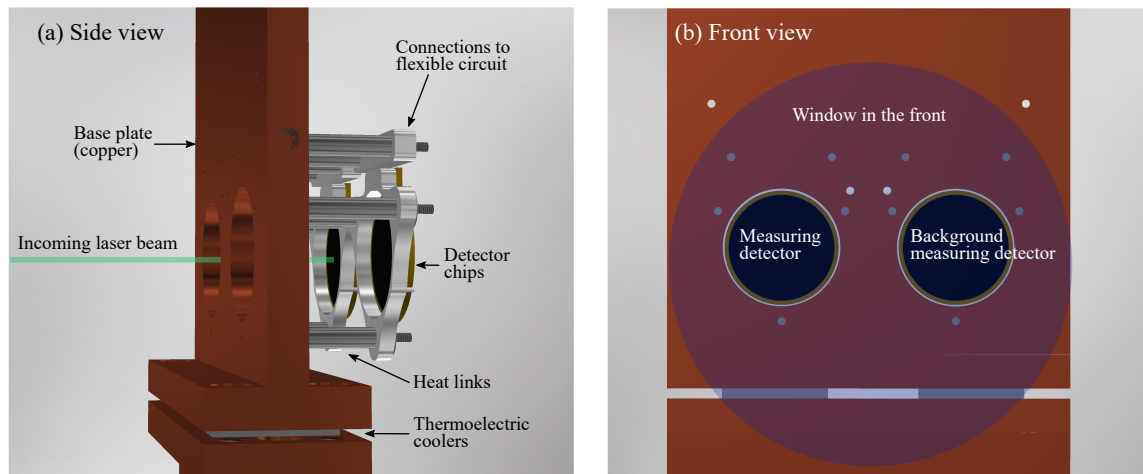


Figure 1: Side view of the modeled PARRoT radiometer (a) and front view looking through the copper block to the detectors (b). Note, the wedge window sits in front of the copper block.

## 2.1 Thermal design

The geometry of the detector chip and the location of thermistors affect the bolometer's performance. Greater spatial symmetry and multiple thermistors placed symmetrically around the absorber results in better spatial uniformity and smaller inequivalence between optical and electrical powers. The two circular detector chips of the proposed bolometer will be microfabricated on a silicon (Si) substrate, each with a diameter of 24 mm and a thickness of 1 mm. The diameter of the VACNT absorber is selected to be 20 mm since the diameters of the laser beams used in the C-series laser power calibration system at NIST vary between 1 mm and 11 mm ( $1/e^2$ ). Thermal analysis of the detector chip is shown in Fig. 2. The detector chip geometry was optimized by minimizing the inequivalence between optical and electrical heating powers using the finite element method (FEM).

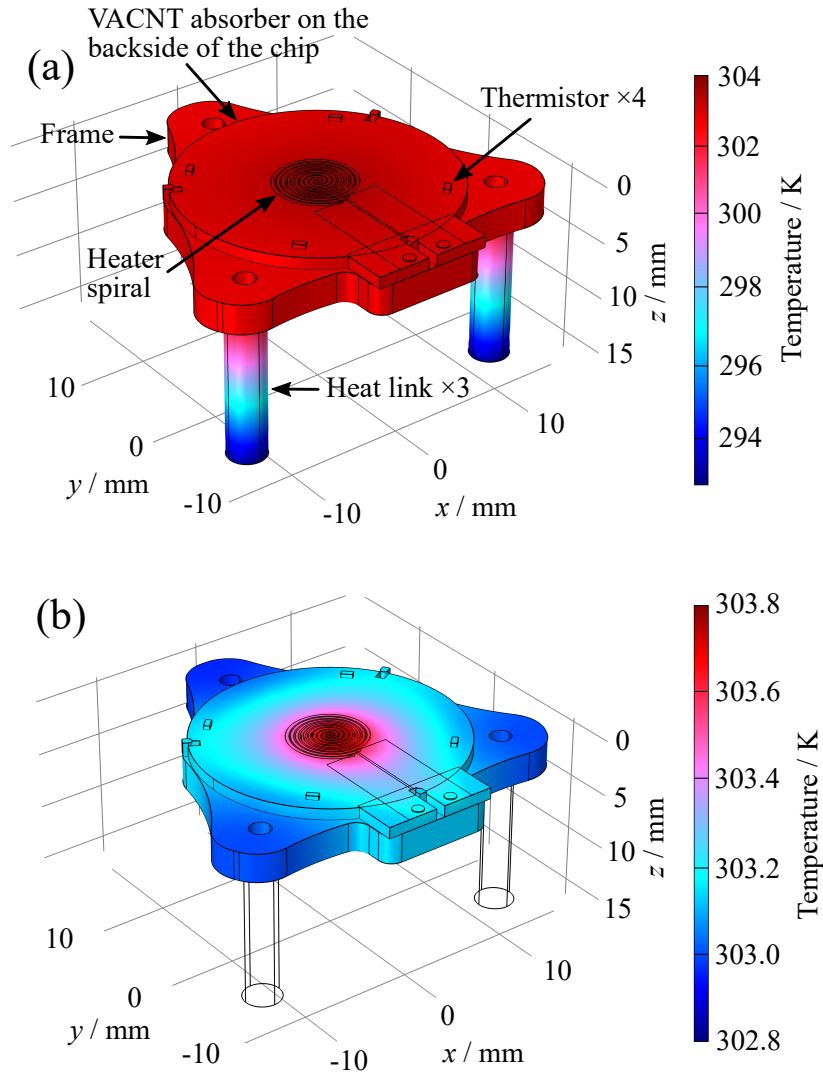


Figure 2: Thermal analysis with an electrical heating mode obtained from COMSOL Multiphysics\* software: (a) is the modeled heat map of the bolometer assembly, and (b) is a higher contrast heat map of the bolometer chip.

The lowest inequivalence would be obtained by placing the electrical heater directly under the optical VACNT absorber. However, currently we cannot grow VACNTs over electrical traces without electrical shorting.<sup>10</sup>

Therefore, the best practical result is obtained by placing the VACNT absorber and the Gaussian heater spiral (details in Appendix A) on opposite faces of the chip. The leads and the heater spiral are selected to be tungsten (W) since it is compatible with VACNT growth at 800 °C.<sup>10</sup> We noted that the spatial uniformity of the inequivalence between optical and electrical powers improves when increasing the thermistors' distance from the center of the absorber since spatial temperature gradients at the edge change less with misaligned laser beam than those in the middle of the detector chip. Four negative-temperature-coefficient (NTC) thermistors, each having 10 k $\Omega$  resistance at 298 K, will be connected electrically in parallel and placed evenly 10 mm away from the center of the heater spiral, near the edges of the detector chip. An insulating layer of silicon dioxide (SiO<sub>2</sub>) with a thickness of 1.2  $\mu\text{m}$  is needed between the semiconducting Si and the heater spiral. In practice, we typically grow equally thick layers of SiO<sub>2</sub> on both faces of detector chips, so the chip geometry in the FEM simulations was modeled accordingly.

Table 1 lists material properties used in thermal simulations. The frame supporting the detector chip is made of aluminum. Three legs forming the weak heat link are solid cylinders made of stainless steel #304 with a thermal conductivity of 14.4 W m<sup>-1</sup> K<sup>-1</sup> at 303 K. In addition to the listed properties in Table 1, the electrical heating of the Gaussian tungsten heater spiral was modeled with Joule heating using the measured electrical resistivity of 150 · 10<sup>-9</sup>  $\Omega \cdot \text{m}$ .

Table 1: List of material properties at 303 K for thermal analysis.

Material	Thermal conductivity / W · m <sup>-1</sup> · K <sup>-1</sup>	Specific heat / J · kg <sup>-1</sup> · K <sup>-1</sup>	Density / kg · m <sup>-3</sup>	Emissivity / unitless
VACNT forest	11.4, 0.114 <sup>a,10,11</sup>	720	41 <sup>10</sup>	0.9996 <sup>5</sup>
Silicon dioxide	1.4	705	2410	–
Silicon	135	856	2329	0.62
Tungsten	175	132	17800	0.02
Aluminum	240	910	2710	–
Stainless steel #304	14.4	500	8000	–

<sup>(a)</sup> Anisotropic: along CNTs ( $z$ -axis), side ways in the VACNT forest ( $xy$ -plane)

The thermal conductivity of the VACNT forest is anisotropic and along the CNTs it can be approximated as the effective thermal conductivity

$$k_{\text{CNT,eff}} = f \cdot k_{\text{CNT}} , \quad (1)$$

where  $k_{\text{CNT}}$  is the thermal conductivity of an individual multi-walled carbon nanotube and  $f$  is the fill factor that can be estimated by measuring and comparing the density of the VACNT forest to that of graphite. In our VACNT forest, the fill factor is  $\sim 1.9\%$ .<sup>10</sup> Since the thermal conductivity of an individual multi-walled CNT is 600 W m<sup>-1</sup> K<sup>-1</sup> along the tube,<sup>11</sup> the effective thermal conductivity of our VACNT forest is approximately 11.4 W m<sup>-1</sup> K<sup>-1</sup>. The thermal conductivity sideways in the VACNT forest is only a small fraction of that along the CNTs because of the low fill factor, and we approximate it to be 100 times lower.

Conductive power loss of the proposed heat link (Fig. 2) is  $\sim 280$  mW when the detector chip is at  $\Delta T = 10$  K higher temperature than the base plate:<sup>6</sup>

$$P_{\text{con}} = G_{\text{con}} \cdot \Delta T, \quad (2)$$

where  $G_{\text{con}}$  (W · K<sup>-1</sup>) is the thermal conductance of the heat link, defined as

$$G_{\text{con}} = N_{\text{cyl}} \cdot \frac{\pi r^2}{l} \cdot k , \quad (3)$$

where  $N_{\text{cyl}} = 3$  is the number of solid cylinders,  $r$  is the radius and  $l$  is the length of a cylinder, and  $k$  is the integrated thermal conductivity (W · m<sup>-1</sup> · K<sup>-1</sup>) of the stainless steel #304 from the base temperature  $T_1 - \Delta T$

to the chip temperature  $T_1$ . The radiative power loss emitted by the detector chip is  $\sim 20$  mW and determined using the Stefan–Boltzmann law as

$$P_{\text{rad}} = \epsilon \sigma A (T_1^4 - T_2^4), \quad (4)$$

where  $\epsilon$  is the emissivity of the surface,  $\sigma$  is the Stefan–Boltzmann constant,  $A$  is the surface area of the detector chip, and  $T_1 = 303$  K and  $T_2 = 295$  K refer to the chip and ambient temperatures, respectively. With the proposed design  $\sim 7\%$  of the heat is dissipated through thermal radiation. This ratio is kept low by coating the frame and the heat link with W because reducing radiative losses reduces radiative coupling with the ambient environment. The corresponding radiative thermal conductance is

$$G_{\text{rad}} = 4\epsilon\sigma AT_1^3. \quad (5)$$

The total thermal conductance consisting of the detector chip and the heat link is

$$G_{\text{tot}} = G_{\text{con}} + G_{\text{rad}} \quad (6)$$

and the corresponding open-loop time constant  $t = 26$  s is calculated from<sup>6</sup>

$$t = \frac{C}{G_{\text{tot}}}, \quad (7)$$

where  $C = c_p \cdot m$  with the specific heat capacity  $c_p$  ( $\text{J} \cdot \text{kg}^{-1} \cdot \text{K}^{-1}$ ) and the mass  $m$  of the Si chip.

### 2.1.1 Spatial uniformity and linearity estimation

When operating the PARRoT radiometer, the temperature of the measuring detector chip follows the temperature of the background measuring detector chip driven by constant electrical heating power. The laser power is measured by the difference in electrical heating power at two different time intervals when the laser is on and off. Since the measuring detector chip is operated in closed loop by electrical heating (Fig. 3) and its temperature is approximately constant, PARRoT is linear within its operation range up to  $\sim 300$  mW.

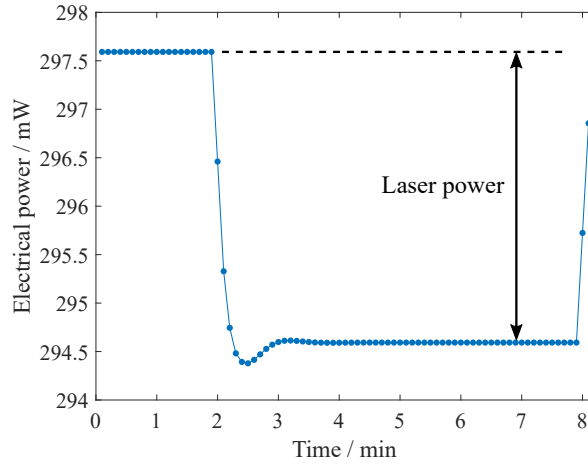


Figure 3: Example of a modeled time-dependent closed loop FEM simulation, in which the laser beam of 3 mW is switched on at the time point of 2 min (and off at 8 min). In the model, the laser beam is aligned perpendicular to the absorber’s center.

The spatial uniformity of the inequivalence between optical and electrical powers obtained by FEM simulations is plotted in Fig. 4 using a 1 mm diameter laser beam of 3 mW power. The geometry of the detector chip and the heat link are adjusted so that the inequivalence is minimized to 0.007% for a perfectly centered laser beam. The spatial uniformity of the inequivalence is within  $\pm 0.02\%$  inside a 4 mm radius from the center of the absorber.

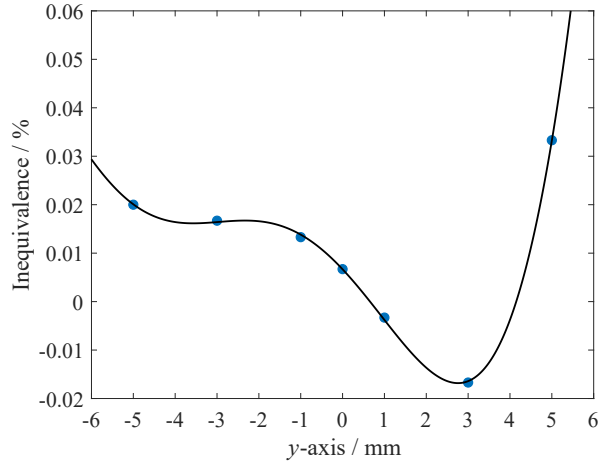


Figure 4: Modeled inequivalence between the optical and electrical powers along  $y$ -axis of the detector chip. Modeling was performed using a laser beam with a radius  $r_{\text{opt}} = 0.5$  mm ( $1/e^2$ ) and power  $P_{\text{opt}} = 3$  mW.

In the simulations, the laser beam was aligned perpendicularly to the absorber's surface with a Gaussian beam distribution defined as

$$I_{\text{opt}}(x, y) = \frac{2P_{\text{opt}}}{\pi r_{\text{opt}}^2} \cdot \exp\left(-\frac{2R^2}{r_{\text{opt}}^2}\right), \quad (8)$$

where  $P_{\text{opt}}$  is the total laser power,  $R = \sqrt{(x - x_{\text{opt}})^2 + (y - y_{\text{opt}})^2}$ ,  $x_{\text{opt}}$  and  $y_{\text{opt}}$  are Cartesian coordinates of the laser beam with respect to the center of the absorber, and the width of the laser beam ( $d_{\text{opt}} = 2 \cdot r_{\text{opt}}$ ) is defined to be within 13.5% ( $1/e^2$ ) from the peak value of the distribution.

## 2.2 Electrical design

### 2.2.1 Compensation of the temperature fluctuations

The temperature of the measuring detector chip is forced to follow the room temperature fluctuations observed by the background compensation detector using a Wheatstone bridge circuit excited by 1 kHz sine wave shown in Fig. 5. When the bridge is balanced, the parallel resistance  $R_{t2}$  of the four NTC thermistors in the measuring detector chip matches with  $R_{t1}$  of the four similar thermistors in the background compensation detector chip as

$$R_{t2} = \frac{R_2}{R_1} R_{t1}, \quad (9)$$

where  $R_1$  and  $R_2$  are 10 k $\Omega$  precision resistors. An AC driven Wheatstone bridge with lock-in detection programmed in the FPGA board allows us to observe small signals below the DC noise floor.

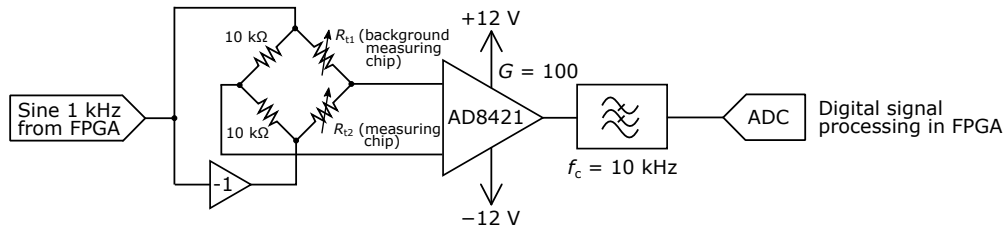


Figure 5: AC driven Wheatstone bridge measurement for balancing temperature of the measuring detector with the background compensation detector.

An alternative method to deal with background temperature fluctuations would be to make the absorber spectrally selective, so that laser wavelengths are absorbed, but radiation near  $10 \mu\text{m}$  is reflected. With the spectrally selective absorber we could remove the background measuring detector which simplifies the mechanical and electrical design of the PARRoT radiometer. Development of a spectrally selective absorber is discussed in Section 4.

### 2.2.2 Measurement of electrical power

The measuring detector chip and the background measuring chip both have their own  $\sim 400 \Omega$  heater spirals. Electrical DC power for each chip is measured separately with a voltage divider over the heater spiral and a  $250 \Omega$  standard resistance, so the electronics contains two circuits of Fig. 6. Voltage across the standard resistor is converted to current that is multiplied by the voltage across the heater to obtain electrical heating power. In the actual measurement, instrumentation amplifiers are used for reducing common mode voltage, and passive voltage dividers consisting of two  $15 \text{ k}\Omega$  precision resistors followed by voltage followers are used for halving the signal within the measurable range of the analog input ( $\pm 10 \text{ V}$ ) of the FPGA board. Prior to measurements, the amplifiers' gains are calibrated against a calibrated volt meter.

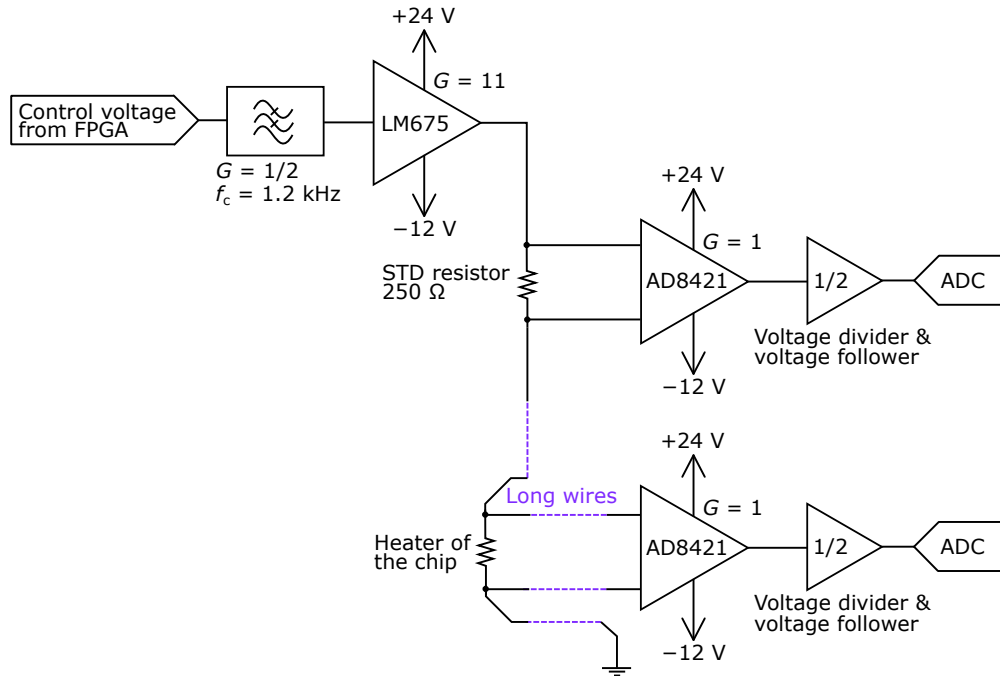


Figure 6: Electrical driving of the heater on the detector chip and the corresponding power measurement. Both detector chips have their own driver and measurement circuits.

## 3. ESTIMATED UNCERTAINTY

We estimate the total expanded uncertainty in laser power measurement with PARRoT to be  $0.063\%$  ( $k = 2$ ) consisting of uncertainty components listed in Table 2. This is a low uncertainty value considering the fact that our radiometer is an absolute thermal detector. Typical uncertainty of room temperature thermal detectors without a background compensation is around  $1\%$ .<sup>2,3,12</sup> Since the PARRoT radiometer is traceable to electrical power, electrical uncertainties arise from calibrations of the standard resistors and voltage gains. Temperature dependence of the standard resistors<sup>13</sup> used in this work is  $\pm 0.00002 \text{ \%}/\text{K}$  being negligible compared to other uncertainties listed in Table 2.

The inequivalence between the optical power and the electrical power was optimized with FEM analysis. The optimized inequivalence corrected from measurement results is  $0.007\%$ , with a standard uncertainty of  $0.0017\%$

arising from the iterative nature of FEM. With an alignment accuracy of  $\pm 1$  mm from the center of the detector, the deviation due to spatial inequivalence is  $\pm 0.01\%$  which corresponds to a standard uncertainty of  $0.0058\%$ . The correction due to the reflectance of the VACNT forest is determined by experimental measurement. The VACNT reflectance which is spectrally dependent is  $\sim 0.04\%$  at  $633$  nm with a standard uncertainty of  $0.0064\%$ .<sup>5</sup> In addition to the aforementioned corrections, the measured laser power has to be divided by the window transmittance. The window transmittance depends on the wavelength, for example at  $633$  nm it is  $\sim 93.17\%$ , being the largest correction factor and also producing the largest uncertainty in the laser power measurement. A standard uncertainty of the window transmittance calibration is  $0.0146\%$  and a standard uncertainty arising from the alignment offset of the laser source and the spatial non-uniformity of the window transmittance is  $0.0173\%$ .

Since the laser beam is aligned at an angle of  $0.5^\circ$  with respect to the front surface normal of the window and perpendicularly to the absorber, both the absorber and the window transmittance are independent of the polarization of the laser beam.

The final component in the uncertainty budget in Table 2 combines both electrical and optical noise since they are indistinguishable in the practical measurement results. For our detector chip the theoretical electrical  $\text{NEP}_{\text{elec}} = \sqrt{4k_{\text{B}}G_{\text{con}}T_1^2} = 0.4$  nW/ $\sqrt{\text{Hz}}$  and optical  $\text{NEP}_{\text{opt}} = \sqrt{8Ak_{\text{B}}\sigma(T_1^5 + T_2^5)} = 0.1$  nW/ $\sqrt{\text{Hz}}$ , where  $k_{\text{B}}$  is the Boltzmann constant and  $A$  is the surface area of the VACNT absorber.<sup>6</sup> The measurement electronics further increases the noise level. In practice, we expect that the remaining power fluctuations which cannot be compensated with the background measuring detector will produce the largest uncertainty. The effect of random noise components can be reduced by a factor of  $1/\sqrt{N}$  by increasing the number of repetition measurements  $N$ . By performing better electrical and window transmittance calibrations, and with more repetitions in laser power measurements, we will try to reduce the total expanded uncertainty ( $k = 2$ ) of the detector down to  $< 0.03\%$ .

Table 2: Estimated uncertainty budget of laser power measurement with PARRoT. The expanded uncertainty with a coverage factor  $k = 2$  corresponds to the confidence level of approximately  $95\%$ .

Uncertainty component	Method	$\pm\delta / \%$	Distribution	Type	$u / \%$
<b><i>Electrical power measurement</i></b>					
Calibration of standard resistance	Experimental	0.002	Normal	B	0.001
Calibration of voltage gain (standard resistor)	Experimental	0.001	Normal	B	0.0005
Calibration of voltage gain (heater of a measuring detector)	Experimental	0.001	Normal	B	0.0005
<b><i>Optical power measurement</i></b>					
Inequivalence between optical and electrical powers	FEM simulation	0.003	Rectangular	B	0.0017
Alignment offset and spatial non-uniformity of absorber	FEM simulation	0.01	Rectangular	B	0.0058
Reflectance of VACNT forest	Experimental <sup>5</sup>	0.011	Rectangular	B	0.0064
Calibration of window transmittance ( $N = 3$ )	Experimental	0.025	Normal	A	0.0146
Alignment offset and spatial non-uniformity of window transmittance	Experimental	0.03	Rectangular	B	0.0173
<b><i>Combined electrical and optical</i></b>					
Measurement repeatability due to noise ( $N = 1$ )	Estimate	0.02	Normal	A	0.02
Combined standard uncertainty ( $k = 1$ ) / %					0.0315
Expanded uncertainty ( $k = 2$ ) / %					0.063

The expanded uncertainty ( $k = 2$ ) stated in Table 2 covers all uncertainties related to the PARRoT radiometer. There will also be uncertainties in calibration or comparison due to laser power instability and selected measurement geometry. For example, if the calibration is carried out by splitting the laser beam to two detectors, there will be uncertainty associated with the beam splitter ratio.

#### 4. TOWARDS SPECTRALLY SELECTIVE BOLOMETERS

Spectral selectivity is a feasible property of the absorbers in room temperature bolometers to reduce radiative coupling with the surrounding environment. Spectral selectivity has been obtained in the past with tandem absorbers,<sup>14</sup> Bragg gratings based on dielectric stacks, and through plasmon resonance in 2D<sup>15,16</sup> and 3D<sup>17</sup> metallic photonic structures. All these structures suffer from a relatively low and spectrally oscillating absorption at the spectral region of interest. In order to use a spectrally selective structure as an absorber material in a primary standard radiometer, its reflectance at the operating spectral region should be the lowest possible, preferably  $<0.05\%$ .

Our goal is to develop a structure with extremely high absorption within the operating spectral region and relatively high reflectance outside the region of interest. We grew VACNT forests on a micropatterned catalyst layer consisting of a  $\sim 2$  nm iron (Fe) layer on a  $\sim 20$  nm aluminum nitride (AlN) layer.<sup>10</sup> The catalyst layer was deposited on top of a  $300 \mu\text{m}$  thick silicon wafer and the backside of the wafer was coated with 100 nm thick W layer. A maskless lithography instrument was used for creating an inverse pattern of the photoresist on top of the catalyst layer. Holes were etched through the catalyst layer by an ion mill. Finally, vertically aligned multi-walled carbon nanotubes were grown on the tiny Fe islands at 2666 Pa, 800 °C, hydrogen–ethylene ratio ( $\text{H}_2:\text{C}_2\text{H}_4$ ) of 1.7:0.2, and flow rate of  $8.3 \text{ cm}^3/\text{s}$ . A top view of the micropatterned VACNT forest is shown in Fig. 7 with thickness  $t = 20 \mu\text{m}$ , hole diameter  $d = 2 \mu\text{m}$ , and pitch size  $\Lambda = 3 \mu\text{m}$ .

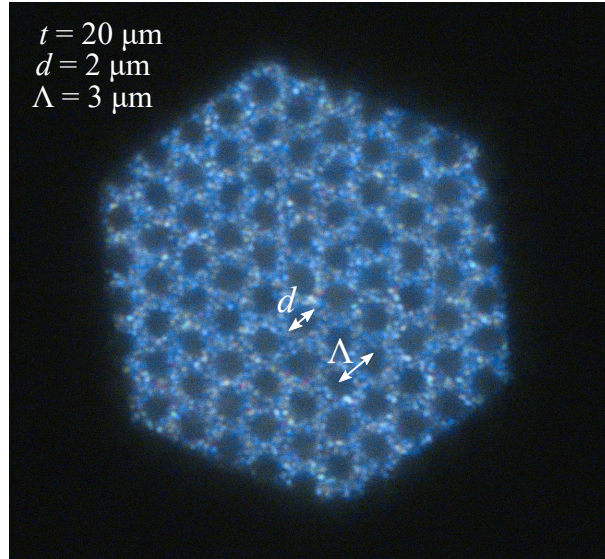


Figure 7: Microscope image of the top view of the micropatterned VACNT forest studied in this work. In the image, the bright areas are VACNTs.

We simulated the spectral reflectances of the patterned VACNT forests using the finite-difference time domain (FDTD) method. The VACNT forests were modeled using the effective refractive index approximation, from the complex refractive index of graphite, with the fill factor  $f$  and the vertical alignment  $x$  (horizontal  $x = 0$ , vertical  $x = 1$ ).<sup>1</sup> When the VACNT fill factor was high, the photonic absorption band was created between  $\Lambda$  and  $2d$  for a square lattice.<sup>18</sup> In the case of a hexagonal lattice, the photonic absorption band was created between  $\frac{\sqrt{3}}{2}\Lambda$  and  $2d$  as seen in Fig. 8. However, decreasing the VACNT fill factor decreased the spectral selectivity.

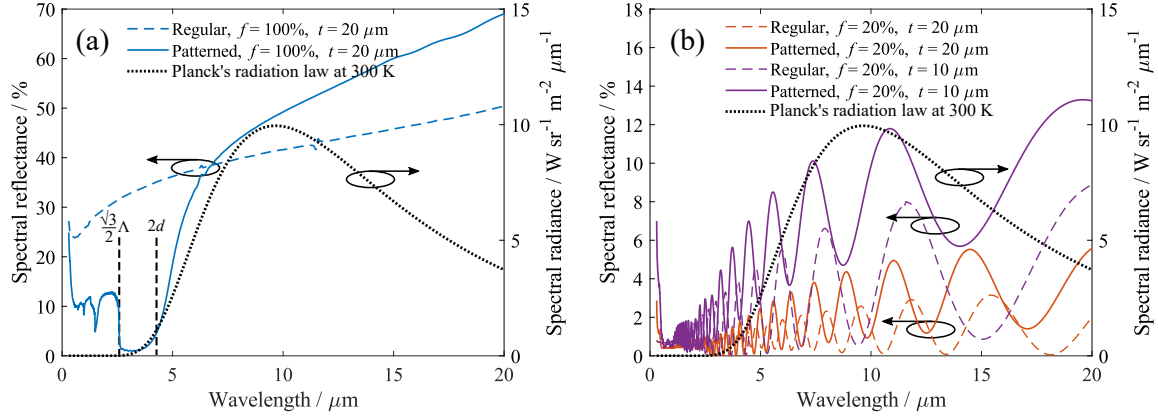


Figure 8: In (a), spectral reflectances of the patterned graphite layer modeled with the FDTD method and the bulk graphite layer modeled with Fresnel equations. In (b), corresponding reflectances for the VACNT forests with  $f = 20\%$  and thicknesses  $t = 10\ \mu\text{m}$  and  $t = 20\ \mu\text{m}$ . The VACNT alignment was set to  $x = 0.99$  in all simulations.

Figure 9 shows the hemispherical spectral reflectances of the patterned and regular VACNT samples measured using Fourier-transform infrared spectroscopy (FTIR) over the spectral range  $1.5\ \mu\text{m} - 16\ \mu\text{m}$ . For the patterned VACNT samples with thickness between  $10\ \mu\text{m} - 20\ \mu\text{m}$ , the spectral reflectance of the samples was  $\sim 10\%$  at the infrared region. For VACNT forests longer than  $20\ \mu\text{m}$ , both the absolute reflectance and the spectral selectivity at the infrared region gradually decreased and the same trend was observed in modeled spectra. We believe the patterning decreases the effective complex refractive index and the increased reflectance was a result of long wavelength photons being transmitted through the VACNT forest and retro-reflected from the tungsten layer. One way to improve spectral selectivity and enhance resonance effects would be to grow denser VACNT forests with a more uniform top surface and possibly coat these structures with reflective metal particles, such as gold or tungsten, similarly as Cui *et al.*<sup>19</sup>

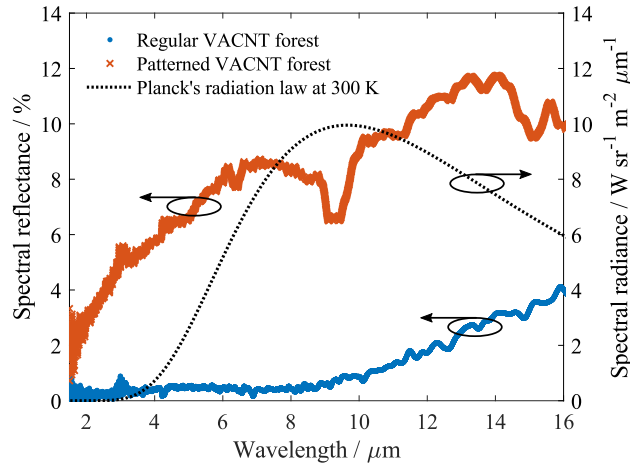


Figure 9: Hemispherical spectral reflectances of the patterned and regular VACNT forests with the same thickness of  $\sim 20\ \mu\text{m}$  measured using FTIR spectroscopy.

## 5. CONCLUSIONS

We have designed a microfabricated bolometer based on a vertically aligned carbon nanotube (VACNT) absorber and an electrical power substitution method. The bolometer will operate at room temperature with a  $20\ \text{mm}$

diameter circular absorber, covering the spectral range from 300 nm to 2300 nm and measuring laser powers up to 300 mW with an expected uncertainty of 0.06% ( $k = 2$ ). With more accurate electrical and window transmittance calibrations than used in our current estimates, an expanded uncertainty of <0.03% should be achievable in the future. The new bolometer will replace NIST's 50 year old cavity-based standard for free-space CW laser power measurements that has an expanded uncertainty of 0.86% ( $k = 2$ ). The proposed bolometer is currently under construction and the results of its performance will be published.

In our bolometer design, we operate the detector in a differential configuration with an identical bolometer to compensate for fluctuations and noise from the laser power results that arise from radiative coupling to ambient temperature. We also studied the possibility of reducing unwanted temperature sensitivity of the bolometer with a spectrally selective VACNT forest grown on top of micropatterned catalyst so that we could simplify the bolometer design by removing the background measuring detector. With the low-density micropatterned VACNT forest containing holes with a diameter of 2  $\mu\text{m}$ , pitch size of 3  $\mu\text{m}$  and thickness 10  $\mu\text{m} - 20 \mu\text{m}$ , we measured the hemispherical spectral reflectance to be 10% at the near infrared region, which was probably associated with the decreased effective refractive index of the patterned VACNT forest.

## APPENDIX A – GAUSSIAN HEATER SPIRAL

The heater spiral consists of two Archimedean spirals with 180° phase difference and varying lead width. The inner edge of the first spiral (0°) is defined as

$$x_{1,1} = (a + b\theta_1) \cdot \cos(\theta_1) \quad (10)$$

$$y_{1,1} = (a + b\theta_1) \cdot \sin(\theta_1) \quad (11)$$

and the outer edge of the first spiral is obtained by varying the width of the heater wire by Gaussian function as

$$x_{1,2} = x_{1,1} + \left( c \cdot \left[ 1 - \exp\left(-\frac{r_1^2}{2\sigma^2}\right) \right] + d \right) \cdot \cos(\theta_1) \quad (12)$$

$$y_{1,2} = y_{1,1} + \left( c \cdot \left[ 1 - \exp\left(-\frac{r_1^2}{2\sigma^2}\right) \right] + d \right) \cdot \sin(\theta_1) \quad (13)$$

where  $r_1 = \sqrt{x_{1,1}^2 + y_{1,1}^2}$ . The second spiral (180°) is obtained by replacing  $\theta_1$  with  $\theta_2 = \theta_1 + \pi$  and  $r_1$  with  $r_2 = \sqrt{x_{2,1}^2 + y_{2,1}^2}$  in Eqs. (10–13). The parameters for our heater spiral in Fig. 2 were selected to be  $a = 0 \mu\text{m}$  (offset from the origin),  $b = 120 \mu\text{m}$  (growth rate of the spiral),  $d = 60 \mu\text{m}$  (minimum width of the spiral), and  $c + d = 360 \mu\text{m}$  (maximum width of the spiral). Parameter  $\sigma = 1800 \mu\text{m}$  describes how the lead width of the Gaussian heater spiral changes with respect to the distance from the center of the spiral. The first branch of the spiral is designed to have 4 rounds and the second branch to have 4.5 rounds. One way of adjusting the resistance of the spiral without changing its shape is to vary the thickness of the W leads.

## ACKNOWLEDGMENTS

A.V. thanks Jenny and Antti Wihuri Foundation, Finland for the post-doctoral grant that made this research possible.

\*Certain commercial equipment, instruments, or materials are identified in this paper in order to specify the experimental procedure adequately. Such identification is not intended to imply recommendation or endorsement by the National Institute of Standards and Technology, nor is it intended to imply that the materials or equipment identified are necessarily the best available for the purpose.

## REFERENCES

- [1] J. Lehman, C. Yung, N. Tomlin, D. Conklin, and M. Stephens, “Carbon nanotube-based black coatings,” *Applied Physics Reviews* **5**, 011103-1–17 (2018).
- [2] E. D. West and K. L. Churney, “Theory of Isoperibol Calorimetry for Laser Power and Energy Measurements,” *Journal of Applied Physics* **41**, 2705–2712 (1970).

- [3] E. D. West, W. E. Case, A. L. Rasmussen, and L. B. Schmidt, “A Reference Calorimeter for Laser Energy Measurements,” *Journal of Research of the National Bureau of Standards – A. Physics and Chemistry* **76A**, 13–26 (1972).
- [4] N. A. Tomlin, M. White, I. Vayshenker, S. I. Woods, and J. H. Lehman, “Planar electrical-substitution carbon nanotube cryogenic radiometer,” *Metrologia* **52**, 376–383 (2015).
- [5] M. G. White, Z. E. Ruiz, C. S. Yung, I. Vayshenker, N. A. Tomlin, M. S. Stephens, J. H. Lehman, “Cryogenic Primary Standard for Optical Fibre Power Measurement,” *Metrologia* **55**, 706–715 (2018).
- [6] P. L. Richards, “Bolometers for infrared and millimeter waves,” *Journal of Applied Physics* **76** 1–24 (1994).
- [7] E. N. Glezer, A. E. Lange, and T. M. Wilbanks, “Bolometric detectors: optimization for differential radiometers,” *Applied Optics* **31**, 7214–7218 (1992).
- [8] D. Harber, Z. Castleman, G. Drake, S. Van Dreser, N. Farber, K. Heuerman, M. Miller, J. Rutkowski, A. Sims, J. Sprunck, C. Straatsma, I. Wanamaker, W. Zheng, G. Kopp, E. Richard, P. Pilewskie, N. Tomlin, M. Stephens, C. Yung, M. White, J. Lehman, “Compact total irradiance monitor flight demonstration,” *SPIE Conference Proceedings* **11131**, 111310D-1–8 (2019).
- [9] J. G. Ziegler and N. B. Nichols, “Optimum settings for automatic controllers,” *Transactions of the ASME* **64**, 759–768 (1942).
- [10] N. A. Tomlin, C. S. Yung, Z. Castleman, M. P. Denoual, G. Drake, N. Farber, D. Harber, K. Heuerman, G. Kopp, E. Richard, J. Rutkowski, J. Sprunck, M. Stephens, C. Straatsma, S. Van Dreser, I. Vayshenker, M. G. White, S. I. Woods, W. Zheng, and J. H. Lehman, “Microfabricated carbon nanotube bolometers,” (in preparation).
- [11] A. E. Aliev, M. H. Lima, E. M. Silverman, and R. H. Baughman, “Thermal conductivity of multi-walled carbon nanotube sheets: radiation losses and quenching of phonon modes,” *Nanotechnology* **21**, 035709-1–11 (2010).
- [12] R. J. Phelan Jr. and A. R. Cook, “Electrically Calibrated Pyroelectric Optical-Radiation Detector,” *Applied Optics* **12**, 2494–2500 (1973).
- [13] Vishay Precision Group, Inc. “Ultra High Precision Z Foil Through-Hole Resistor,” (Datasheet 2014).
- [14] N. Selvakumar, S. B. Krupanidhi, and H. C. Barshilia, “Carbon Nanotube-Based Tandem Absorber with Tunable Spectral Selectivity: Transition from Near-Perfect Blackbody Absorber to Solar Selective Absorber,” *Advanced Materials* **26**, 2552–2557 (2014).
- [15] V. Rinnerbauer, E. Lausecker, F. Schäffler, P. Reininger, G. Strasser, R. D. Geil, J. D. Joannopoulos, M. Soljačić, and I. Celanovic, “Nanoimprinted superlattice metallic photonic crystal as ultrasensitive solar absorber,” *Optica* **2**, 743–746 (2015).
- [16] V. Rinnerbauer, Y. X. Yeng, W. R. Chan, J. J. Senkevich, J. D. Joannopoulos, M. Soljačić, and I. Celanovic, “High-temperature stability and selective thermal emission of polycrystalline tantalum photonic crystals,” *Optics Express* **21**, 11482–11491 (2013).
- [17] J. G. Fleming, S. Y. Lin, I. El-Kady, R. Biswas, and K. M. Ho, “All-metallic three-dimensional photonic crystals with a large infrared bandgap,” *Nature* **417**, 52–55 (2002).
- [18] J. Chiu and W.-B. Young, “Theoretical Approach to Simulate Efficient Selective Solar Absorbers With Micro or Nano Structured Arrays,” *Materials Research* **21**, e20171026-1–8 (2018).
- [19] K. Cui, P. Lemaire, H. Zhao, T. Savas, G. Parsons, and A. J. Hart, “Tungsten–Carbon Nanotube Composite Photonic Crystals as Thermally Stable Spectral-Selective Absorbers and Emitters for Thermophotovoltaics,” *Advanced Energy Materials* **8**, 1801471-1–9 (2018).